

Article

Effect of the Size of the Superhydrophobic Regions of Biphilic Surfaces on the Bubble Dynamics

José Pereira ^{1,*}, Ricardo Cautela ¹, Ana Moita ^{1,2} and António Moreira ¹

¹ IN+ Center for Innovation, Technology and Policy Research, Instituto Superior Técnico, Universidade de Lisboa, Av. Rovisco Pais, 1049-001 Lisboa, Portugal; ricardo.m.cautela@tecnico.ulisboa.pt (R.C.); anamoita@tecnico.ulisboa.pt (A.M.); aluismoreira@tecnico.ulisboa.pt (A.M.)

² CINAMIL—Centro de Investigação Desenvolvimento e Inovação da Academia Militar, Academia Militar, Instituto Universitário Militar, Rua Gomes Freire, 1169-203 Lisboa, Portugal

* Correspondence: sochapereira@tecnico.ulisboa.pt

Abstract: The current work aims to experimentally evaluate the effect of the size of circular superhydrophobic regions of biphilic surfaces on the bubble dynamics under pool boiling conditions. Biphilic surfaces are structured surfaces with tunable wettability, presenting an array of hydrophobic small spots in a hydrophilic surface or vice versa. The factors that affect the bubble dynamics are of geometric nature such as the diameters of the bubbles, their volume, and the height of the centroid, and of more complex nature such as the departure frequency of the bubbles and the rate of evaporation mass transfer. In this study, the bubble dynamics and boiling performance were evaluated by adjusting the diameter of the single circular superhydrophobic regions. A stainless steel AISI 304 foil was used as the base hydrophilic region, and the superhydrophobic regions were made by spray coating the NeverWet[®] superhydrophobic solution over well-defined masks. The main conclusion was that the bubble dynamics are clearly affected by the diameter of the superhydrophobic spots. The smaller spots favored the generation of more uniform and stable bubbles, mainly due to the border surface tension forces' dominance. With the increase in the diameter of the bubbles, the surface tension acting at the border with the much larger hydrophilic region impacts the process less. Thus, the smaller superhydrophobic regions had higher evaporation mass transfer rates. The region with the best pool boiling performance along with improved bubble dynamics was the superhydrophobic region with an 0.8 mm diameter, corresponding to a superhydrophobic area to total area ratio of 0.11%. Moreover, this experimental work confirmed that the bubble dynamics' impacting factors such as the diameter at the various stages of development of the bubbles can be modulated according to the final objectives of the design and fabrication of the biphilic surfaces. The research significance and novelty of this work come from the comprehensive study of the geometrical pattern of the heat transfer surface in pool boiling conditions and its impact on the bubble dynamics and heat transfer capability. We also suggest further studies considering nanoscale superhydrophobic spot arrangements and the future usage of different working fluids such as nanofluids.

Keywords: heat transfer; nucleate boiling; biphilic surfaces; bubble dynamics



Citation: Pereira, J.; Cautela, R.; Moita, A.; Moreira, A. Effect of the Size of the Superhydrophobic Regions of Biphilic Surfaces on the Bubble Dynamics. *Symmetry* **2023**, *15*, 949. <https://doi.org/10.3390/sym15040949>

Academic Editors: Sergei D. Odintsov and Chih Ping Tso

Received: 2 March 2023

Revised: 12 April 2023

Accepted: 20 April 2023

Published: 21 April 2023



Copyright: © 2023 by the authors. Licensee MDPI, Basel, Switzerland. This article is an open access article distributed under the terms and conditions of the Creative Commons Attribution (CC BY) license (<https://creativecommons.org/licenses/by/4.0/>).

1. Introduction

Nowadays, the scientific community working in this field is perfectly aware that the two-phase nucleate boiling regime is one of the most efficient heat dissipation processes. This regime exhibits a considerably improved heat transfer performance, especially when compared with the single-phase heat transfer procedures. Hence, the two-phase pool boiling is used in a wide variety of purposes and technologies, which require the removal of high heat fluxes, including the cooling and thermal stabilization of high-power electronic components and systems [1], thermal and nuclear power plants [2], thermal desalination

systems [3], aviation and space equipment [4], cryogenic engineering [5], and thermal management procedures based on the vaporization and condensation cycles using heat pipes, heat exchangers, and thermosyphons [6]. The pool boiling process depends on a considerable number of factors including the temperature, pressure, and intrinsic thermophysical characteristics of the working fluid, and heating surface morphology and properties. In certain cases, an alteration in one of these factors may lead to serious consequences in the heat transfer behavior and in the nucleate boiling crisis and may even lead to the erosion or corrosion of the equipment in practical situations. These factors are also directly linked with the achievable heat transfer coefficient (HTC) and critical heat flux (CHF) of the boiling system, since they affect the saturation point of the operating fluid, nucleation active sites' density, nucleation frequency, and postponing of the onset pool boiling. Moreover, the most common strategies to enhance the HTC and CHF are based on the modification of the heating surface, either by changing its morphology through structuring at micro- and nanoscale or by tuning its wettability. In this sense, the first studies examining the nucleate pool boiling heat transfer enhancement proposed, for instance, machining procedures to modify the heating surface [7], the formation of re-entrant cavities [8], and porous coatings [9]. The main conclusion of these approaches was related to increases in the HTC and CHF during the pool boiling process on such surfaces, which were caused by the formation of more nucleation sites and additional vapor trapping in the re-entrant cavities. The fast development of nanotechnologies in the past few years has significantly provided more feasible options for surface modification, especially at nanoscale, which have been explored by various researchers to develop novel processes for boiling performance improvement. All these works demonstrated that the usage of modified enhanced surfaces at nanoscale led to a noticeable heat transfer enhancement caused by the augmented vapor entrapment and thin liquid film evaporation in the pores. Both effects can reduce the surface superheating degree for a given working heat flux. Simultaneously, the stability and durability of the coatings are still relevant concerns, given that they can make difficult, or even impede, the implementation of one surface modification technique in practical applications. Because of this, the search for the most adequate coating configuration and fabrication techniques to improve the boiling heat transfer continues today. Nonetheless, in this direction, Shi et al. [10] developed a multifunctional aviation aluminum alloy with improved superhydrophobicity and corrosion resistance through a two-step process of etching followed by polymer modification. The superhydrophobicity was achieved after the polymer modification with fluorsilane, and the contact angle increased by about 101° after the etching process. Additionally, the corrosion resistance of the metallic alloy increased by up to 83.2% after etching for 7 min. The authors stated that the superhydrophobic character of the surface appreciably enhanced its liquid repellence, leading to an improved counter corrosion capability. Additionally, this type of surface should be applied in future pool boiling studies. Another possible way to control the heat transfer during the pool boiling process is to alter the wettability of the heating surface [11]. Particularly, the boiling process on hydrophobic surfaces, with a contact angle superior to 90° , can be characterized by an appreciable decrease in the onset of nucleate boiling (ONB) [12]. On the other hand, the usage of a hydrophilic heating surface, with a contact angle inferior to 90° , results in an increment in the CHF during the boiling process [13]. This is the rationale behind the interest of the scientific community recently directed to the utilization of surfaces with heterogeneous wettability, usually designated by biphilic surfaces. Hence, many authors [14–18] have performed boiling heat transfer studies on the wettability of heterogeneous heating surfaces to take advantage of the wettability gradient effect by a mixture of hydrophilic and hydrophobic properties. The appeal of biphilic surfaces comes fundamentally from the decrease in the ONB and, at the same time, increase in the HTC and CHF during the pool boiling process. Moreover, Lim et al. [19] studied the diameter and position of the vapor bubbles by changing the size of the hydrophobic regions on the hydrophilic surface. The researchers found that the bubble departure diameter decreased with decreasing size of the hydrophobic regions, and the CHF increased with decreasing bubble departure diameter.

Additionally, Jo et al. [20] reported that the HTC enhancement on biphilic surfaces was due to the rapid ONB on the hydrophobic regions and the absence of waiting time caused by the remaining vapor bubbles on the hydrophobic regions after the detachment stage. Additionally, Betz et al. [21] showed that the mixed hydrophilic and hydrophobic surfaces enhanced both HTC and CHF by performing experiments on hydrophilic networks (hydrophilic surface with circular hydrophobic regions) and hydrophobic networks (hydrophobic surface with circular hydrophilic regions). The authors reported that the hydrophilic networks had the best performance in preventing the formation of an insulating vapor blanket. Additionally, Motezakker et al. [22] conducted pool boiling experiments on hydrophilic surfaces with different hydrophilic to hydrophobic region ratios and found that the optimal ratio was around 38.5%. Furthermore, Sun et al. [23] studied the boiling dynamics and heat transfer during the pool boiling of biphilic surfaces composed of a silica oxide hydrophilic surface and polytetrafluorethylene (PTFE) rectangular hydrophobic spots. The researchers concluded that the nucleation site density of the biphilic surface was much higher than that of the constitutive homogeneous surfaces. Hence, more than 70% of the hydrophobic spots could be activated with a heat flux of 206 w/cm^2 . Additionally, it was confirmed that the bubbles nucleated on the interface of the hydrophobic and hydrophilic regions and, after that, moved into the middle of the hydrophobic regions. Hence, the circular hydrophobic spots played the role of improved active nucleation sites for the bubbles to grow until their departure from the surface. The bubble departure periods scattered between 80 ms and around 1500 ms. Similarly, Xia et al. [24] investigated the influence of the surface wettability on the bubble formation and motion of superhydrophilic and superhydrophobic homogeneous surfaces, as well as biphilic surfaces with symmetrically arranged superhydrophobic regions in the superhydrophilic base region. The different surfaces were obtained by the surface laser texturing ablation technique and by sililation grafting to obtain superhydrophobic characteristics. The authors reported that the surface wettability had an appreciable role in the bubble formation, growth, and departure. Once again, on the developed biphilic surface, the bubbles spread toward the superhydrophobic region under the driving force provided by the Laplace pressure difference. The vapor bubbles generated on the superhydrophilic region close to the biphilic boundary could be displaced and spread into the superhydrophobic region when the bubbles contacted the superhydrophobic boundary, which in turn induced the horizontal motion of the vapor and surrounding fluid. Moreover, Serdyukov et al. [25] developed a biphilic surface to improve the pool boiling in a vacuum. They used a sapphire hydrophilic surface and NeverWet[®] solution spray-coated hydrophobic spots. The results showed that the biphilic surface provided a significant increase in the number of detached bubbles over time when compared to that of a bare sapphire surface under the same pressure range. It was also reported that, under a pressure of 10 kPa, the bubble departure diameters during the pool boiling of the biphilic surface were six times lower than the ones of the bare hydrophilic surface. Additionally, it was found that for sub-atmospheric pressures inferior to 39 kPa, the departure frequency of the bubbles increased considerably compared to that using the bare sapphire surface. The results revealed that, in contrast with the bare surface, the boiling curves for the biphilic surface coincide with each other during the pressure variation between 10 kPa and 39 kPa. Moreover, an appreciable near-four-fold HTC enhancement was reported for the biphilic surface compared to the one verified with the bare surface. Recently, Liu et al. [26] studied the boiling heat transfer in hydrophilic and hydrophobic copper surfaces. The research team found that at low heat fluxes, the HTC of the hydrophobic surface was higher than that of the hydrophilic surface, whereas at high heat fluxes, the opposite took place. The heat transfer capability modification caused by the wettability is due to the bubble growth behavior difference in these surfaces. At low heat fluxes, the bubbles on the hydrophobic surface presented an extended growth period and enlarged diameter at departure, which are features that augment the heat transfer capability since the phase change can continuously proceed. As the heat fluxes increased, the large contact area between vapor and heating surface turned into an obstacle to the heat transfer on the hydrophobic surface; hence, its HTC became lower than that

of the hydrophilic surface. Additionally, the large vapor areas on the surface may break the vapor channel, leading to a precocious deterioration of the heat transfer performance. All the mentioned published studies aim to obtain the ideal parametric configuration for CHF enhancement and heat-transfer-improved capability of the biphilic surfaces under pool boiling regimes. Nevertheless, some fundamental issues need further investigation and more complete understanding. This is the reason for the search for an optimal configuration for a biphilic surface that enables a maximum HTC and CHF during the pool boiling process. According to the aforementioned published studies, the influencing factors of the optimal arrangement are mainly the number and location of the superhydrophobic spots, the size of the spots, the pitch between the spots, and the ratio of hydrophobic to hydrophilic areas, which are all factors closely linked with the bubble and vaporization dynamics of the biphilic surfaces. In addition, there are already some publications proposing optimal configurations for biphilic surfaces at atmospheric pressure [27,28]. However, the number of published scientific articles concerning the influence of the experimental parameters on the dynamics of the vapor bubbles during the pool boiling of biphilic surfaces is still relatively low. Particularly, factors such as the nucleation frequency of the bubbles and their departure diameters remain somewhat poorly understood. Once again, it should be emphasized further comprehensive research in this field using modern measuring techniques is required. Furthermore, more studies are required on the pool boiling processes of biphilic surfaces that use nanofluids, such as the one by Kamatchi and Venkatachalapathy [29]. Additionally, some practical applications in the electronics cooling field using heat exchangers, such as the one described by Kannan and Kamatchi [30], should be further addressed. Accordingly, the current experimental work's goal is to study the effect of different configurations of a biphilic surface composed of a hydrophilic stainless-steel foil and Neverwet™ spray formulation producing superhydrophobic spots on the heat transfer performance during water pool boiling at atmospheric pressure. The aim is to obtain the optimum diameter of the superhydrophobic arrangements in the biphilic surfaces, which enables the general amelioration of the pool boiling characteristics and the CHF enhancement. This work intends to contribute a parametric study for nucleate boiling heat transfer enhancement. Additionally, it suggests further research studies with the use of nanofluids and nanoscale superhydrophobic regions. Figure 1 shows some of the parameters and forces involved in the nucleation and growing of a symmetrically shaped bubble in a superhydrophobic region.

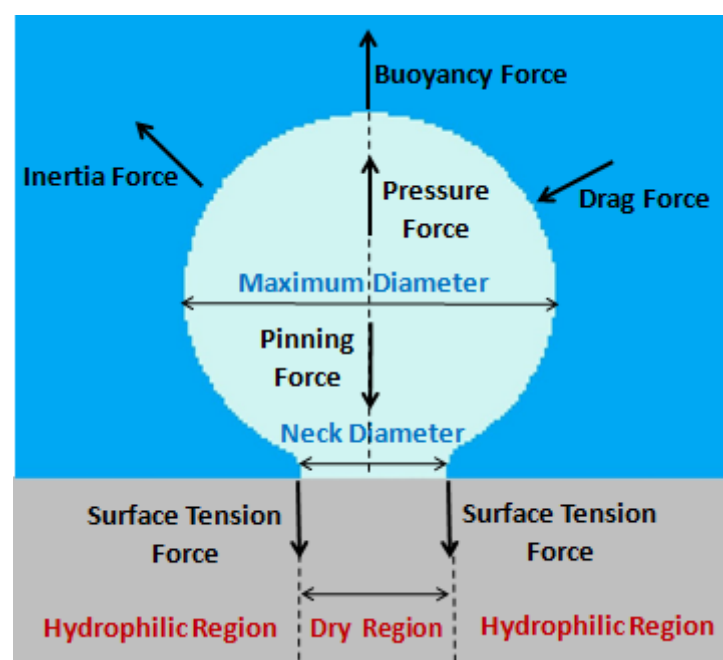


Figure 1. Scheme of the forces involved in a bubble generated in a superhydrophobic region.

2. Materials and Methods

The pool boiling experiments were performed using an in-house developed pool boiling setup, which is schematically represented in Figure 2. The detailed pool boiling chamber scheme is presented in Figure 3. All the experiments were conducted at saturation temperature and atmospheric pressure (1 bar) using distilled water (DW) as the working fluid. The DW was introduced into the boiling chamber and was heated and kept at the saturation temperature of 100 °C with the aid of a proportional-integrative-derivative (PID) control system that regulated the power output of a cartridge heater. This element together with two electric resistances and a coil heater kept the DW at the required temperature. The pressure and temperature of the DW were monitored by an OMEGA DYNE INC pressure transducer and two-type K thermocouples. One thermocouple was placed near the heat transfer surface and connected to a DAQ reader, and the other thermocouple was positioned close to the heat resistance and connected to the PID controller. The heat transfer surface was a 20 µm-thick stainless steel AISI 304 rectangular foil with dimensions of 50 × 32 mm², which was heated by Joule effect by regulating the electric current provided by a HP62748 DC power supply. The bottom size of the testing surface was painted using a high-emissivity black matt paint. The heat losses were evaluated by performing an energy balance on the stainless-steel foil with the pool boiling chamber empty, and they were found to be at most around 20% for the higher applied heat fluxes. We took high-speed images of the bubble dynamics on the biphilic surfaces using a PhantomTM v4.2 camera from Vision Research positioned in front of the glass chamber window. The frame rate of the camera was set to 2200 fps and the relation mm/pixel used was 0.040 mm. The high-speed imaging observation and analysis were obtained from extended-time experiments with a duration of 20 min. The total number of detached bubbles from the heating surface in this period was counted for 40.5 s every 2 min. The departure frequency of the bubbles was determined as the total number of detached bubbles during this period of 40.5 s. Such procedure involving long-term periods was employed to infer the repeatability of the events and obtained results, assuring that the short-term measurements of 10 s that were performed next were not affected by the different bubble departure frequencies, which could occur at longer time intervals due to, for instance, pressure variations. For each biphilic surface test, we applied four different electric current values between 3A and 9A, which allowed us to impose heat fluxes to the heat transfer surface between 0.025 W/cm² and 0.229 W/cm². All the data were recorded under steady-state conditions when the fluctuations in data from the sensors became negligible. The waiting time to reach the steady-state condition depended on the applied heat flux. We carried out experiments on one single circular superhydrophobic region with diameters ranging between 0.8 mm and 5.2 mm. For each set of experimental conditions, we conducted five experiments to characterize the evolution of the contact angle of the bubbles, maximum diameter, base diameter, height of the centroid, volume of the bubbles, departure frequency, and evaporation mass transfer rate. An average of the data from these five experiments was taken to obtain representative plots and results. The dynamic images were analyzed using a post-processing in-house developed MATLAB routine. Additionally, all the measures were post-processed by the border detection algorithm of this routine.

2.1. Uncertainties

Table 1 presents the measurement uncertainties considered in this work. The calculated uncertainties are summarized along with the uncertainties provided by the manufacturers.

Additionally, the MATLAB routine was used for quantifying the bubble dynamics parameters and associated uncertainties. According to the report in [31], the uncertainties associated with the determination of the diameter of the bubbles (Δd) depends on factors such as the pixel-to-millimeter conversion factor (C_f) and associated error (ΔC_f), and the detection of the border of the bubble-associated error (edb). Considering a pixel-to-millimeter conversion uncertainty of $\pm 5\%$ and a detection of the border uncertainties

of ± 2 pixels, the uncertainties associated with the diameter of the bubbles can be given by Equation (1):

$$\frac{\Delta d}{d} = \sqrt{\left(\frac{\Delta C_f}{C_f}\right)^2 + \left(\frac{2e_{db}}{dC_f}\right)^2} \quad (1)$$

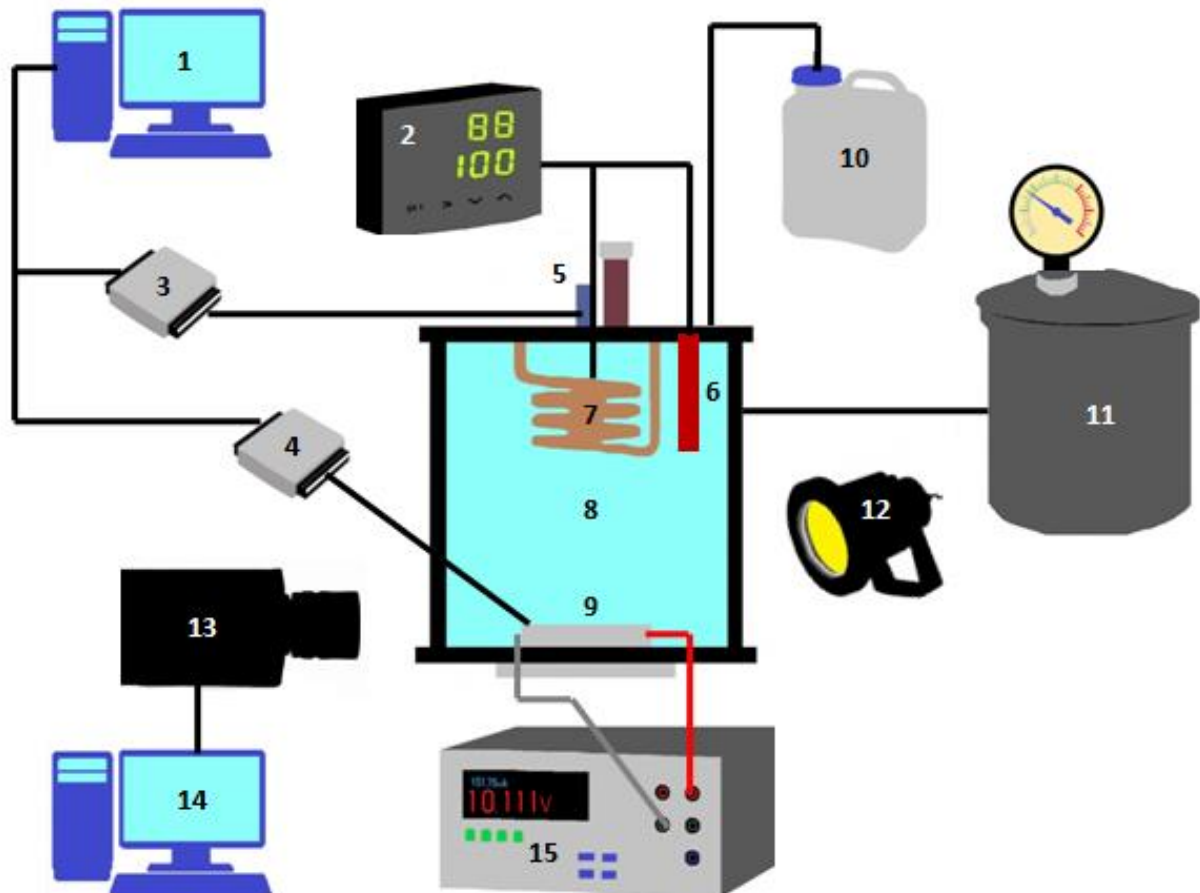


Figure 2. Scheme of the in-house developed setup: 1—PC 1, 2—PID controller, 3—DAC 1, 4—DAC 2, 5—Pressure transducer, 6—Cartridge heater, 7—Coil heater, 8—Pool boiling chamber, 9—Sample holder, 10—Condensate container, 11—Degassing station, 12—Light projector, 13—High-speed camera, 14—PC 2, 15—DC voltage source.

Table 1. Uncertainties associated with the experimental parameters.

Parameter	Uncertainty
Voltage	± 1 V
Electric Current	± 0.5 A
Surface Temperature	± 1.2 °C
Working Fluid Temperature	± 1.0 °C
Pressure (OMEGA DYNE sensor)	± 1.6 mbar
Operating Fluid Volume	± 10 mL
Bubble Departure Frequency	± 0.025 Hz
Bubble Departure Radius	± 0.05 mm
Bubble Departure Volume	± 0.05 mm ³
Contact Angle (theta tensiometer)	± 0.1 °
Image Pixel Size	0.040 mm

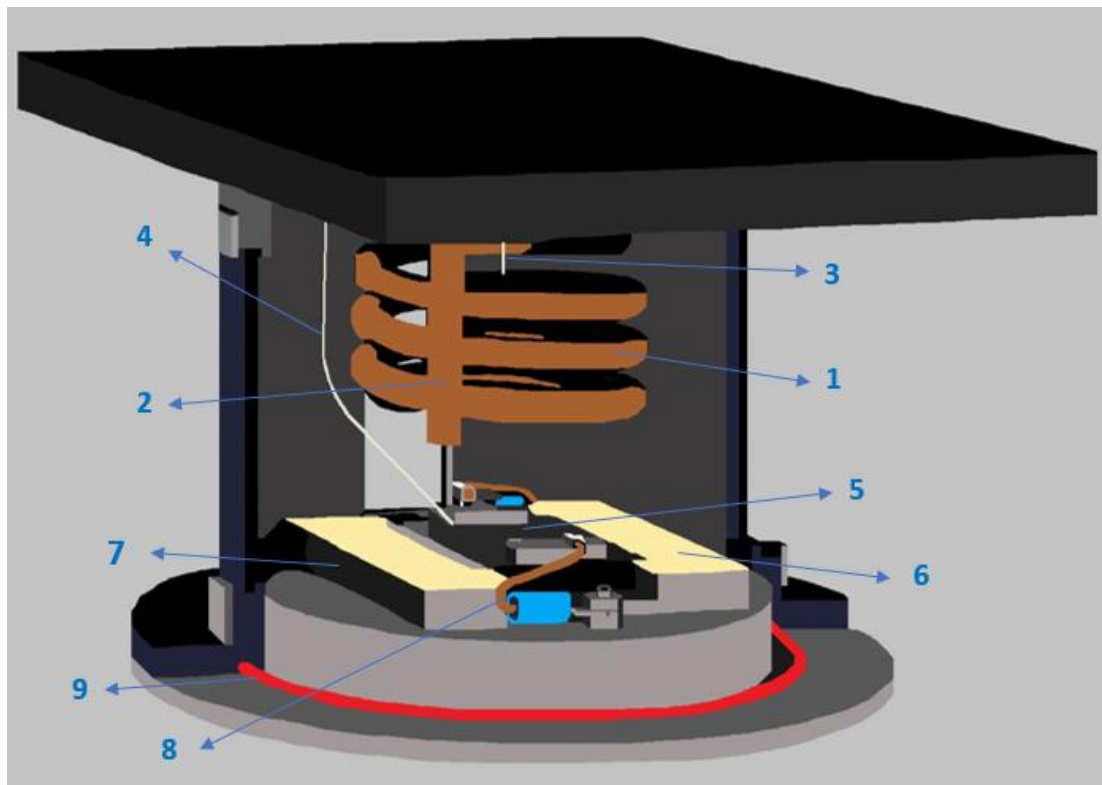


Figure 3. Scheme of the more detailed pool boiling chamber with the main components: 1—Heating coil, 2—Heating cartridge, 3, 4—Type K thermocouples, 5—Testing Surface, 6—Kapton[®] insulating tape, 7—Testing surface base, 8—Copper wire, 9—O-ring.

Table 2 shows the relative errors associated with the bubble dynamics parameters in the largest superhydrophobic region with a diameter of 5.2 mm for an imposed heat flux. The summarized values served as a reference for all the tested superhydrophobic regions. The parameter d_{\max} is the maximum diameter of the bubbles, θ_{\min} is the minimum dynamic contact angle of the bubbles, y_{cmax} is the maximum height of the centroid of the bubbles, and V_{\max} is the maximum volume of the bubbles.

Table 2. Bubble-dynamics-parameters-associated uncertainties for the superhydrophobic region with a diameter of 5.2 mm at constant heat flux.

Region Diameter (mm)	$e[d_{\max}]$ (%)	$e[\theta_{\min}]$ (%)	$e[y_{\text{cmax}}]$ (%)	$e[V_{\max}]$ (%)
5.2	7.8	10.6	18.5	13.0

Table 3 presents the relative errors associated with the mean departure frequencies measured in the largest superhydrophobic region with a diameter of 5.2 mm for four different imposed current intensities. It should be stated these errors are not negligible and reveal some degree of imprecision in the frequency results. Nevertheless, the summarized values served as a reference for all the tested superhydrophobic regions.

Table 3. Departure-frequencies-associated uncertainties for the superhydrophobic region with a diameter of 5.2 mm for four different imposed currents.

Region Diameter (mm)	$e[f_{3A}]$ (%)	$e[f_{5A}]$ (%)	$e[f_{7A}]$ (%)	$e[f_{9A}]$ (%)
5.2	-	25.5	16.4	10.0

2.2. Design and Preparation of the Biphilic Surfaces

All the testing types of biphilic surfaces were fabricated on $50 \times 38 \times 0.020$ mm³ AISI 304 stainless steel foils. The foils were profoundly cleaned in a bath of 99% pure acetone before each test. Then, the foils were fixed with silicone onto a thermal glass wafer. The superhydrophobic spots were made using a mask of polyvinyl chloride (PVC) insulating tape with a well-defined circular hole with variable diameters. After that, we spray deposited, step-by-step, five or more coating layers of the superhydrophobic spray formulation NeverWet™ from RustOleum™. This formulation showed robustness after being submitted to successive heating and cooling cycles, keeping its integrity without noticeable cracks or relevant wettability changes. The second to the fifth coating layer were applied after 30 min of drying of the last applied coating. Hence, the PVC tape worked as a template for the superhydrophobic regions in the stainless-steel hydrophilic surface. After 12 h of the deposition of the last coating layer, the tape was removed, revealing well-defined circular superhydrophobic spots. The stainless steel superhydrophobic spots' surrounding areas were carefully cleaned again with acetone. To find the effect of the size of the superhydrophobic circular spots, the diameter of the spots was gradually enlarged until a maximum value was reached. Since the current work intended to evaluate the bubble dynamics of a single vapor bubble, the biphilic testing configuration was composed by the hydrophilic stainless-steel surface and only one superhydrophobic spot with variable diameter. We used six different spot diameters of 0.8 mm, 1.3 mm, 2.4 mm, 3.6 mm, 4.4 mm, and 5.2 mm. Table 4 summarizes the geometric characteristics of the used biphilic surfaces.

Table 4. Geometric characteristics of the biphilic testing surfaces.

Surface Number	Superhydrophobic Spot Diameter ϕ (mm)	Superhydrophobic Area/ Total Area Ratio A (%)
1	0.8	0.11
2	1.3	0.28
3	2.4	0.95
4	3.6	2.14
5	4.4	3.20
6	5.2	4.47

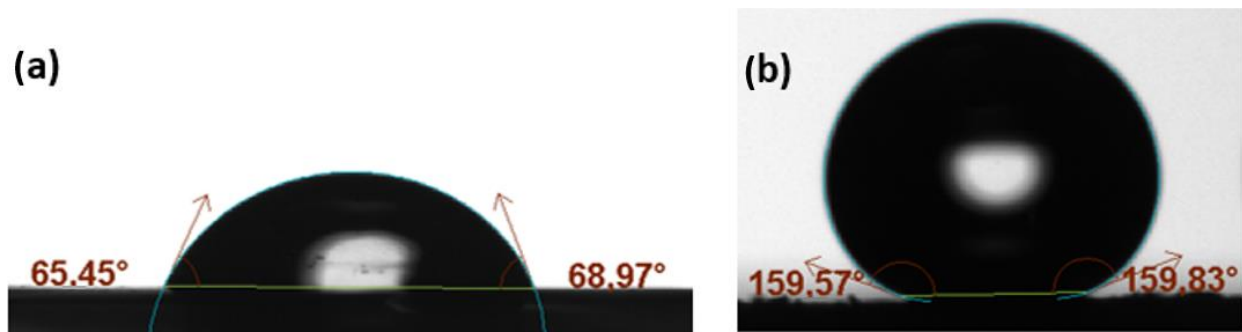
2.3. Wettability Determination of the Biphilic Surfaces

The biphilic surfaces were characterized by their wettability, evaluated through the static water contact angle measurement by optical tensiometry. Hence, the equilibrium static contact angle (θ) was measured using the THETA™ tensiometer from Attension. A DW sessile drop of 5 μ L was deposited at room temperature on the hydrophilic and superhydrophobic surfaces, and a 10 to 12 fps video was captured by the OneAttension v. 4.1 software. This software uses a drop detection algorithm, which is based on the Young–Laplace equation. The procedure to obtain the final contact angle value involved the value averaged over at least ten different measurements from representative areas of the surfaces. The final average values of the measured contact angles and corresponding standard deviations (SDV) are shown in Table 5. Figure 4 illustrates the contact angle measurements for both regions of the biphilic surface. Previous work, e.g., [14,32], checked for possible aging effects based on contact angle measurements before and after the experimental tests. The results did not show any significant change in the wettability which could be related to surface aging.

The values summarized in Table 5 show that the regions covered with the NewerWet™ spray solution presented a clear superhydrophobic behavior with a contact angle superior to 150°, and that the stainless-steel foil presented a hydrophilic nature with a contact angle inferior to 90°.

Table 5. Measured contact angles of the biphilic surfaces' superhydrophobic and hydrophilic regions.

Region Wettability	Material	Number of Measuring Points	Contact Angle θ ($^{\circ}$)	\pm SDV ($^{\circ}$)
Superhydrophobic	NeverWet™ Formulation	10	151.6	2.6
Hydrophilic	Stainless steel AISI 304	10	63.7	3.3

**Figure 4.** Water contact angle measurement for: (a) stainless steel biphilic region and (b) NeverWet™ superhydrophobic region.

2.4. Surface Roughness Determination of the Biphilic Surfaces

The surface roughness of the biphilic surfaces was characterized by a Dektak3-Veeco profilometer with a maximum vertical resolution of 200 Å. The obtained roughness profiles were then processed to determine the average roughness R_a and average peak-to-peak roughness R_z , which is the average of the highest peaks of the profile according to the DIN4768 standard. The corresponding average values after at least five measurements, together with the respective standard deviation for the superhydrophobic region, were of $R_a = 5.8 \pm 1.5 \mu\text{m}$ and $R_z = 22.6 \pm 3.9 \mu\text{m}$. The stainless-steel hydrophilic substrate resulted in near-zero R_a and R_z values within the resolution of the equipment. Hence, the surface roughness of the stainless-steel hydrophilic region was negligible.

3. Results and Discussion

One of the main objectives of the present work was the production of biphilic surfaces with only one superhydrophobic region with a variable diameter. This procedure resulted in a more accurate evaluation of the bubble dynamics. We also intended to develop superhydrophobic spot matrixes with a diameter of less than 1 mm. First, we evaluated the dynamic behavior of the bubbles. Figure 5 presents the different stages of the development of the bubbles generated in the largest tested circular superhydrophobic region with a diameter of 5.2 mm. The figure shows the high-speed images of the fundamental evolution stages of a bubble from its nucleation to its departure from the heat transfer surface: the nucleation stage, hemisphere formation, vertical elongation, departure beginning, necking, and departure or detachment from the heating surface. On the first image on the left, the bubble is at the early nucleation stage after the departure of the preceding bubble, and the corresponding nucleation waiting time is 5 ms. As seen in the second and third images, the bubble formed a hemisphere, which is vertically elongated in the two following images. This effect is due to the prevalence of the impulsion forces over the adhesion forces present. It should be noted that the growing of the bubble is restricted to the superhydrophobic region and, consequently, the relative weight of the surface tension forces can be attributed to the geometry and size of that region. Additionally, the boundary region between the hydrophilic and superhydrophobic regions of the biphilic surface also has a considerable influence on the set of the forces present. In the period between 1200 ms and 1225 ms,

the departure of the bubble started, and the surface tension forces promoted the necking of the base of the bubble, which gradually developed until the departure of the bubble. On the two following images corresponding to 1260 ms and 1270 ms, the departure of the bubble is eminent, with only a small connection between the base of the bubble and its upper part, resulting from a sharp necking. This necking of the base of the bubble promotes, by the vapor mass conservation law inside the bubble, an acceleration of the vapor to the zone of the bubble, which results in a complete detachment of the bubble from the heating surface. At the moment of departure, 1280 ms, a vapor layer was left behind on the superhydrophobic region. This time evolution of the bubble is consistent with findings reported by Teodori et al. [33]. It is also proper to state that the last stages of the evolution of the bubble were carried out in a very short period, 80 ms, as compared to the total time required for the nucleation and development of the bubble. The vapor mass left deposited on the heating surface may be due to the fact that in the superhydrophobic region, there is no solid–vapor–liquid surface tension component that favors the detachment of that vapor mass from the surface. Hence, and considering that the nucleation of a bubble in a superhydrophobic region can occur at a temperature between 1 °C and 3 °C higher than the saturation temperature, the fast nucleation and coalescence of microscale bubbles produces a continuous vapor film over the superhydrophobic region. These mechanisms were also detailed by Malavasi et al. [34] and Teodori et al. [35].

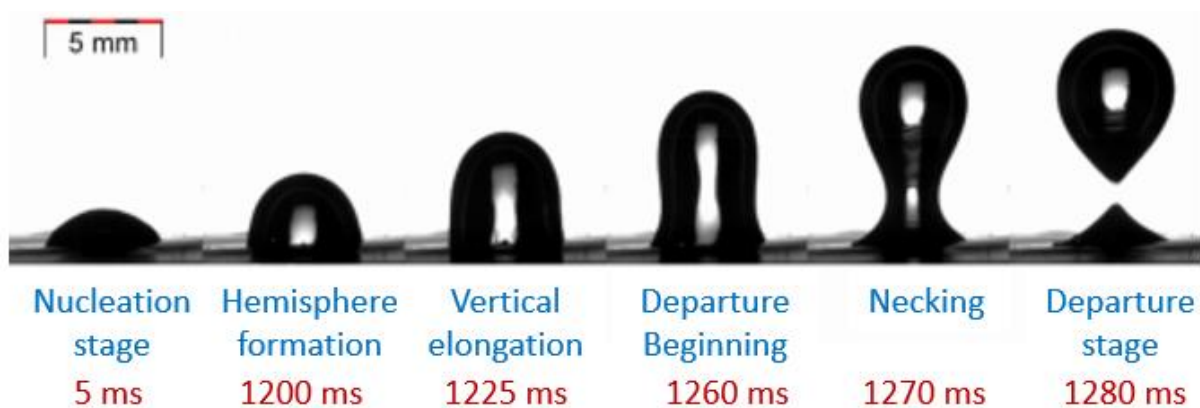


Figure 5. Image sequence showing the evolution of the generated bubbles in the superhydrophobic region with a diameter of 5.2 mm.

In sum, the bubble diameter is constrained by the diameter of the circular superhydrophobic spot, growing up to the limit of the boundaries between the superhydrophobic spot and the remaining hydrophilic surface. Additionally, given that there are no surface tension forces acting on the superhydrophobic spots contributing to the detachment of the bubble, these forces mainly act at the boundary of the superhydrophobic spots. Therefore, for smaller superhydrophobic spots, the necking occurs earlier, and the departure frequency of the bubbles increases. As the bubble detaches from the heating surface, the superhydrophobic spots are instantly covered by a new vapor layer, and there is no quenching promoted by the rewetting of the liquid on the superhydrophobic spots. Nevertheless, the liquid in the larger hydrophilic region may flow, promoted by the bubble departure and coalescence processes. Moreover, the bubble departure frequency and the bubble diameter are affected by the balance between the adhesive forces related to the surface tension at the boundary of the superhydrophobic spots and the buoyancy forces, which are also linked to the size of the superhydrophobic spots. The balance of the forces in play may affect the interaction or coalescence of the vapor bubbles and, consequently, contribute to the latent heat of evaporation and induced heat transfer by convection. Additionally, we observed a larger bubble departure diameter in the larger superhydrophobic areas, which can be explained by the fact that in these larger areas, the surface tension forces act only in the boundary of the superhydrophobic/hydrophilic regions. Hence, the bubble grows freely

in the superhydrophobic spot, and the surface tension forces can also act at later growth stages, delaying the detachment of the bubbles. Furthermore, it should be noted that it has already been demonstrated that the superhydrophobic regions attract the vapor, thus contributing to the onset of nucleate boiling just 1–3K above saturation, as reported by Malavasi et al. [34] and Teodori et al. [35]. Hence, the superhydrophobic regions act as nucleation sites, where boiling starts just 1–3K above saturation. The maximum superheating values obtained for the range of imposed heat flux and for the configuration used here are of the order of 4K–8K (e.g., [14,32]). Furthermore, the bubbles stay constrained inside the hydrophobic regions, as observed in the present work. Nonetheless, it can be stated that the superheating at the boiling surface can affect the shape and dynamics behavior of the vapor bubbles. A high superheat may lead to the formation of large and unstable bubbles, which are more difficult to control than smaller bubbles. The general effects of an increased superheat on the shape and behavior of the bubbles in film boiling are influenced by several factors such as the geometry of the heat transfer surface, thermophysical properties of the operating fluid, and the specific superheating conditions. At high superheats, the bubbles present irregular shapes, which can affect the heat transfer capability of the system and the behavior of the vapor film. Moreover, at high superheats, a second bubble of small size is formed immediately after the detachment of the first bubble. After that, a third bubble of small size is formed, and after a very small fraction of time, the first and second bubble coalesce and merge into a larger bubble. This one detaches from the surface, and a new bubble with the same dimension is formed as the third one detaches from the surface. This bubble dynamics pattern continues with the detachment of more bubbles, disturbing the vapor film and leading to an enhanced heat transfer capability. At high superheats, a large amount of vapor is generated, and the bubbles burst with different sizes, forming a vapor blanket over the heating surface, inducing film boiling or Leidenfrost boiling. Additionally, the high values of the superheat lead to the rapid formation of vapor, which causes the attachment of the bubbles to the vapor blanket. In addition, the increase in the superheat implies an increase in the bubble detachment frequencies. Superheating plays a very important role in augmenting the frequency of the detachment of the bubbles, thereby increasing the heat flux. The imposed heat flux vs. superheat curves for the hydrophilic region and superhydrophobic region, with a diameter of 5.2 mm, of the biphilic surface are presented in Figure 6.

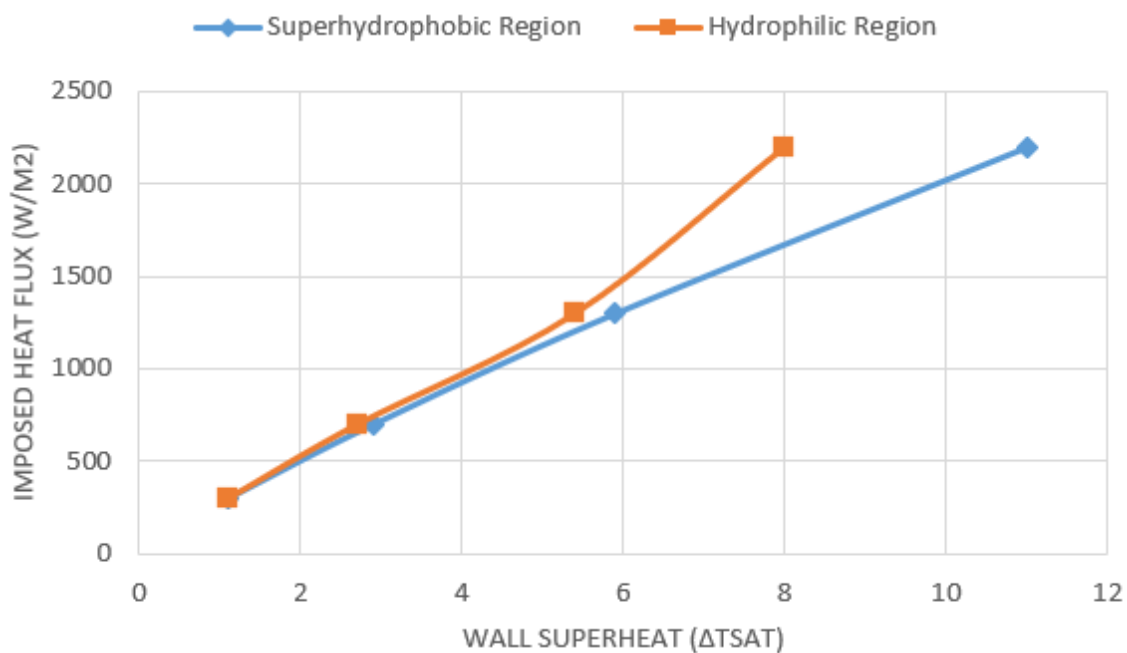


Figure 6. Pool boiling curves for the hydrophilic region and superhydrophobic region with a diameter of 5.2 mm on the biphilic surface.

The heat flux was controlled and kept at low values, always in early stages of nucleate boiling so that bubbles only appeared on the superhydrophobic region and nowhere else. That is the purpose of using the superhydrophobic region in a biphilic surface. It can be observed from the plot in Figure 6 that for heat fluxes values lower than 1300 w/m^2 , the superheat of the hydrophilic region and that of the superhydrophobic region were practically the same. In the case where the imposed heat flux was higher than 1300 w/m^2 , the superhydrophobic region exhibited a higher superheat than that of the hydrophilic region. This occurs due to the continuous presence of vapor in the superhydrophobic region right after the onset of boiling. This effect, which has been widely reported in the literature, including our previous works, assures that the superhydrophobic region is the nucleation site and that there is no nucleation in other unwanted and stochastic places. Playing with their location is then possible by pumping fresh fluid into the hydrophilic region as the bubbles leave the surface, keeping the overall superheat values low (which is beneficial for cooling purposes). Hence, for heat fluxes superior to 1300 w/m^2 , the presence of the superhydrophobic region enhances the heat transfer capability, which is the main reason for the enhanced heat transfer when using superhydrophobic heating surfaces or biphilic surfaces. Due to the early-onset nucleate boiling and this superheat, bubbles were restricted to hydrophobic regions, and if we put them in a pattern, as the bubbles left these hydrophobic regions, they did not coalesce or coalesced far away from the surface, enough to promote the pumping of fresh fluid into the hydrophilic region, so the biphilic surface had a higher heat flux for a low superheat (we see that only the superhydrophobic region increased the superheat, but overall in low values). Nevertheless, if the heat flux is excessive, one observes an increased bubble coalescence, and a vapor film forms in both superhydrophobic and hydrophilic regions, limiting the flow of fresh fluid and, consequently, leading to a reduction in the heat transfer coefficient compared to that of a bare homogeneous hydrophilic surface. This effect is in agreement with that previously reported and clearly shown in [36]. The following figures show the plots of the evolution of the bubble dynamics' influencing parameters of biphilic surfaces with a single superhydrophobic spot. For the acquisition of the plots, we applied a crescent electric current between 3A and 9A, thus obtaining the different heat fluxes between 0.03 W/cm^2 and 0.22 W/cm^2 . In the X axis of the first set of plots, we used the nondimensional time t^* given by Equation (2):

$$t^* = \frac{t}{t_{max}} \quad (2)$$

where t is the time and t_{max} is the maximum time required for the bubbles to reach their maximum base diameter for each value of imposed heat flux. This nondimensional time t^* is used to minimize the discrepancies in the obtained frequencies for each case. It is also worth mentioning that the curves of the plots are the result of the average of at least four repeated experiments for applied current intensities of 3A, 5A, 7A, and 9A, which correspond to heat fluxes of 0.03 W/cm^2 , 0.07 W/cm^2 , 0.13 W/cm^2 , and 0.22 W/cm^2 . Thereafter, we present the results according to the influencing factors of the bubble dynamics of biphilic surfaces with a single superhydrophobic spot. The superhydrophobic spots had the following diameters: 0.8 mm, 1.3 mm, 2.4 mm, 3.6 mm, 4.4 mm, and 5.2 mm. The analyzed parameters were the contact angle, base of the bubble diameter, maximum bubble diameter, centroid height, and volume of the bubble. Figure 7 illustrates the evolution of the contact angle as a function of the non-dimensional time. From Figure 7, it is possible to confirm that the contact angle of the generated bubbles decreased with the decreasing superhydrophobic spot diameter. For instance, the superhydrophobic region with a diameter of 1.3 mm generated bubbles with contact angles inferior to 70° , whereas the 5.2 mm-diameter region formed bubbles with contact angles equal or superior to 110° . It can also be verified that in the early growing stages of the bubbles, the decreasing of the contact angle was less pronounced in the superhydrophobic spots with larger diameters. This was likely due to the slower enlargement of the diameter of the bubble occurring in the larger superhydrophobic

spots. The contact angle evolution was determined by the balance between the impulsion forces and the surface tension forces. In the absence of the surface tension component, which contributes more to the necking stage of development, the bubbles generated in the larger superhydrophobic regions tended to keep growing without any restriction, along with their base diameter. In the earliest stage of the formation of the bubbles, the contact angle inside the bubbles was near 140° . This angle decreased sharply as the bubbles grew until a gradual stabilization occurred, which began at $t^* = 0.25$ during the hemisphere-like growing. The contact angle remained almost constant until $t^* = 0.85$, which marked the beginning of the departure stage of the bubbles. After this time value, the contact angle increased gradually. When the contact angle surpassed 90° , the necking of the base of the bubble commenced and the angle increased significantly in a very short time. At the moment of the complete detachment of the bubble from the heating surface, the contact angle again reached 140° . The evolution of the contact angle of the bubbles was not affected by the heat flux and exhibited some similarity with the evolutions reported for a hydrophilic surface by Phan et al. [37], and those recently reported for a superhydrophobic surface by Teodori et al. [33]. On the one hand, the verified stabilization plateau during a long period had already been reported by Teodori et al. [35]. At this stage, the growing of the bubble was promoted only by the vapor layer produced in the superhydrophobic region and not by the solid–vapor–liquid surface tension in the perimeter of the superhydrophobic region and at the boundary with the hydrophilic region. On the other hand, at the initial and final stages of the growing evolution of the bubbles, these are subjected to the surface tension at the interface between the hydrophilic and superhydrophobic region and, consequently, the involved mechanisms are comparable with the ones observed at the same stages for bubbles generated in hydrophilic surfaces by Phan et al. [37]. Nevertheless, the bubbles which were generated in the smaller superhydrophobic region with a diameter of 0.8 mm displayed the smoothest contact angle evolution, with a difference of only about 10° between the angle of the early growing stage and the departure, indicating the slowest bubble growing rate of all the tested superhydrophobic regions. The noise in the spectral lines is associated with the processing mode of the developed MATLAB algorithm, as well as with some instability and oscillation of the bubbles during their growing. As already reported by Teodori et al. [35], the instability may be the result of three distinct effects. The first one is related to the upward impulsion forces along with the successively lower surface tension forces, which make the bubbles more prone to suffer instabilities from the vapor layer formed at the surface. The second effect is the alteration in the size of the bubbles, which is promoted by the vapor transport between the produced vapor layer and the bubbles. The last one derives from the slowness of the growing process of the bubbles, making them more sensitive to local pressure variations. The second possible effect is less likely to occur in the present situation, since this effect is primarily observed when the vapor layer is much larger than the bubble. In addition, Figure 8 shows the mean base diameter evolution of a generated bubble over time.

The plot in Figure 8 shows that the base diameter of the bubbles reached its maximum when the bubbles totally occupied the corresponding superhydrophobic regions. These results are consistent with the findings of published studies, suggesting that the base diameter of the bubbles is closely related to the area of the superhydrophobic region [38]. It can be stated that the base of the bubbles is confined to its corresponding superhydrophobic region, which is consistent with the reported results, for instance, by Teodori et al. [35]. However, after the vertical elongation stage in the smaller superhydrophobic regions, the bubble grows radially and reaches a dimension that is higher than that of the base. This fact is not noticeable in the larger superhydrophobic regions. Nevertheless, it is possible to verify that the base diameter has its lowest values at the beginning and at the end of the bubble nucleation process, and this effect is more noticeable in the case of bigger bubbles. In addition, in our experiment, the base diameters of the bubbles in all superhydrophobic regions underwent an initial increase until they momentarily stabilized in a near-plateau region. After that, the base diameters decreased in the final stages of the development

of the bubbles until the detachment of the bubbles from the heat transfer surface. The period that the base diameter stayed approximately constant increased as the size of the superhydrophobic region decreased. It is also possible to verify from this plot, as well as from the plot in Figure 9, that the larger the size of the bubble, the bigger the plot line noise. This is likely due to the interference of the preceding bubble in the case of the bigger bubbles. This effect is somewhat attenuated along the development of the new bubble. Figure 9 depicts the mean evolution of the maximum diameter of the bubble over time. This figure shows, in detail, the marked difference in the maximum diameter evolution for the superhydrophobic regions with distinct diameters. It is possible to verify that for the larger superhydrophobic regions, the almost-linear increasing trend in the maximum diameter of the bubbles is gradually replaced by a trend like that of the base diameter evolution over time, which is depicted in Figure 7. The maximum diameter of the bubbles progressively increased and reached, or even surpassed, the value of the corresponding base diameter in the hemispheric growing stage around $t^* = 0.4$ for all the superhydrophobic regions. The slope of the curves seems to be approximately constant until the stages before the departure of the bubbles. The departure can be identified by the steeper decrease in the maximum diameter at around $t^* = 1$. Additionally, the bubbles had their biggest enlargement in the smallest superhydrophobic circular region with a diameter of 0.8 mm, where the mean maximum diameter reached 2.5 mm, which is more than three times greater than the diameter of the corresponding superhydrophobic region.

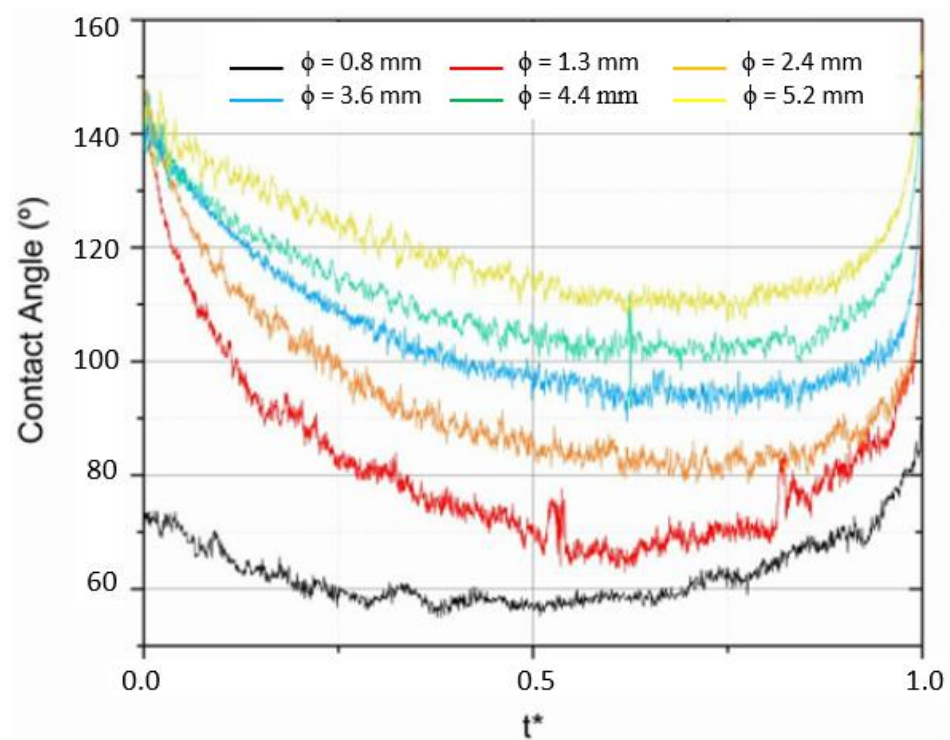


Figure 7. Comparative contact angle time evolution of the generated bubbles in superhydrophobic spots with different diameters.

For both the 0.8 mm- and 1.3 mm-diameter superhydrophobic regions, the maximum diameter of the generated bubbles surpassed the diameter of the region even before $t^* = 0.25$. Additionally, in these regions, the maximum diameter of the bubbles increased linearly until their departure from the heating surface. Moreover, Figure 10 presents the evolution of the ratio between the maximum diameter of the bubble and its base diameter according to the diameter of the superhydrophobic regions. Though the bubbles that were generated in the larger superhydrophobic regions had larger diameters, it can be confirmed that the ratio between the maximum diameter and the base diameter decreased with the increasing

diameter of the superhydrophobic regions. The observed trend suggests that the larger superhydrophobic regions do not necessarily potentiate the transfer of more evaporation mass over time. This fact, together with the departure frequency of the bubbles, determines the amount of latent heat dissipated from the heating surface. Adding the experimental results of two more superhydrophobic regions of 1.5 mm and 2.6 mm diameters, it is possible to observe an exponential trend line.

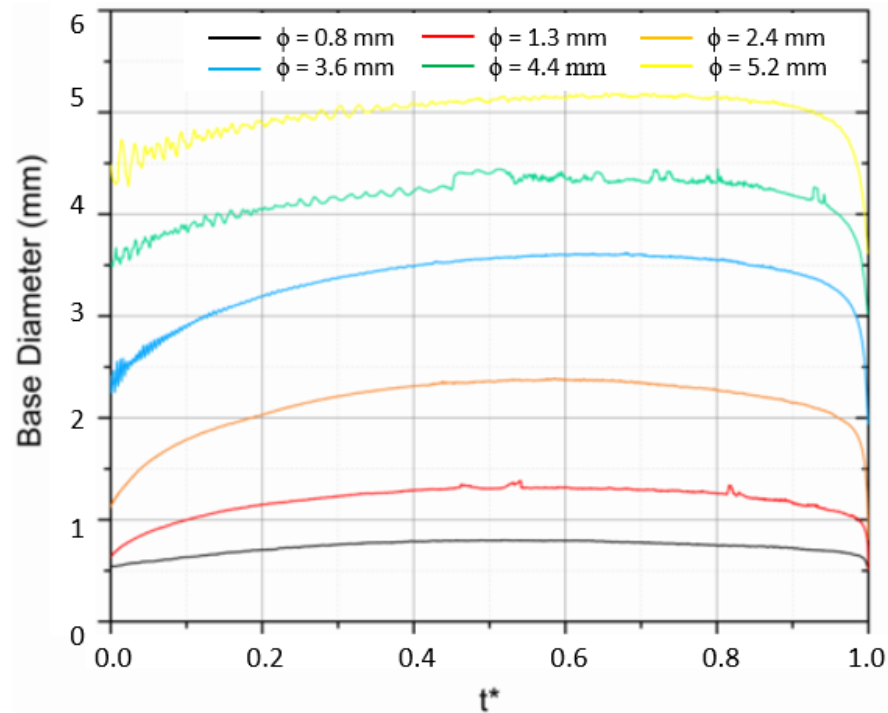


Figure 8. Comparative base diameter time evolution of the generated bubbles in superhydrophobic spots with different diameters.

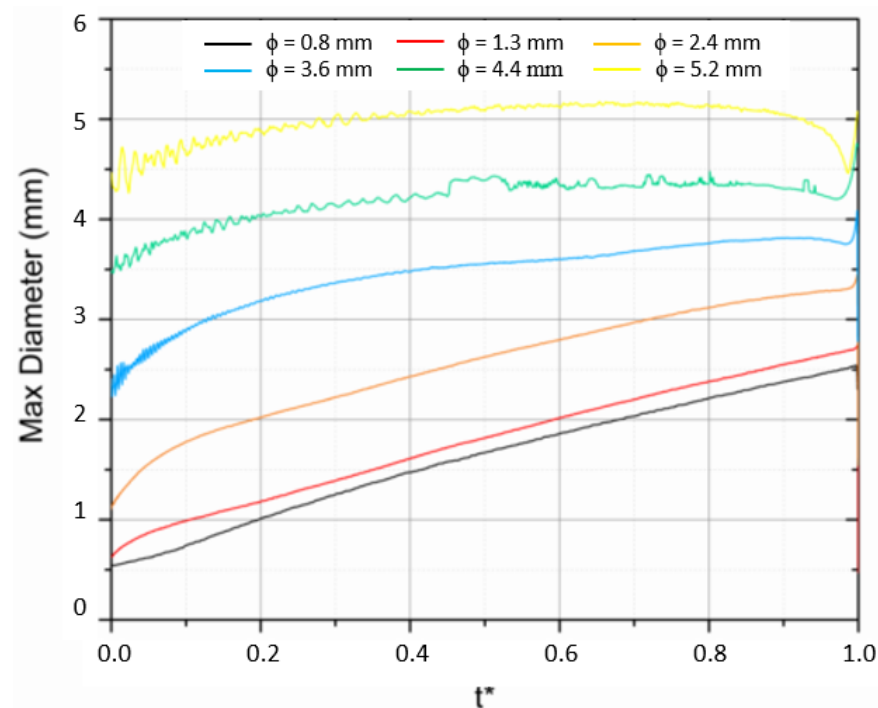


Figure 9. Comparative maximum diameter time evolution of the generated bubbles in superhydrophobic regions with different diameters.

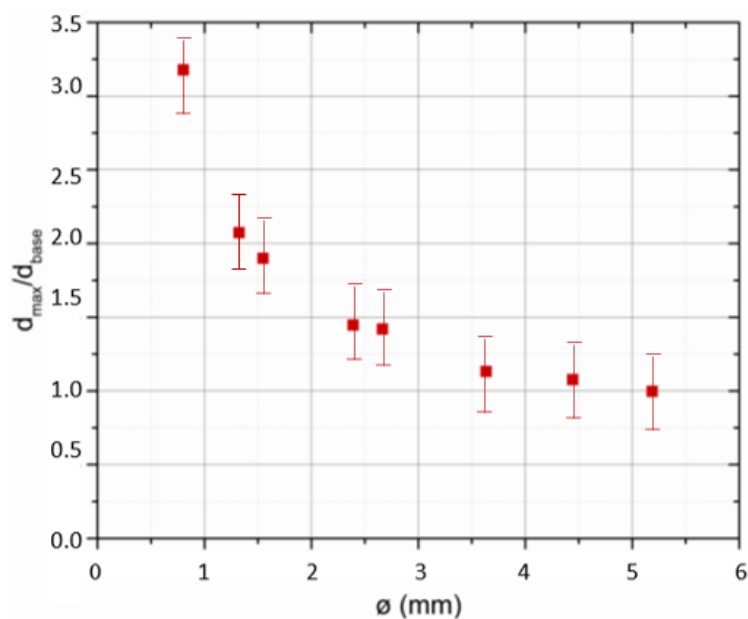


Figure 10. Comparative evolution of the ratio between the maximum diameter of a bubble at departure and its base diameter in the superhydrophobic regions with different diameters (0.8 mm, 1.3 mm, 1.5 mm, 2.4 mm, 2.6 mm, 3.6 mm, 4.4. mm, and 5.2 mm).

Furthermore, in the plot in Figure 11, we can observe the mean evolution over time of the centroid height of the bubbles at the departure stage. We noticed a linear increase in the centroid height of the bubbles until a nondimensional time of 0.85 for all the evaluated superhydrophobic regions. For time values superior to 0.85, all the curves adopted an exponential progress until the departure of the bubbles from the heating surface. In fact, in the necking stage, the height of the geometrical center of the bubbles grew exponentially during the short period of $0.95 < t^* < 1$, until the departure of the bubbles took place. Moreover, the height of the centroid at the departure stage had an average value of 3.5 mm. It was also verified that the height of the centroid evolution was independent of the imposed heat flux value.

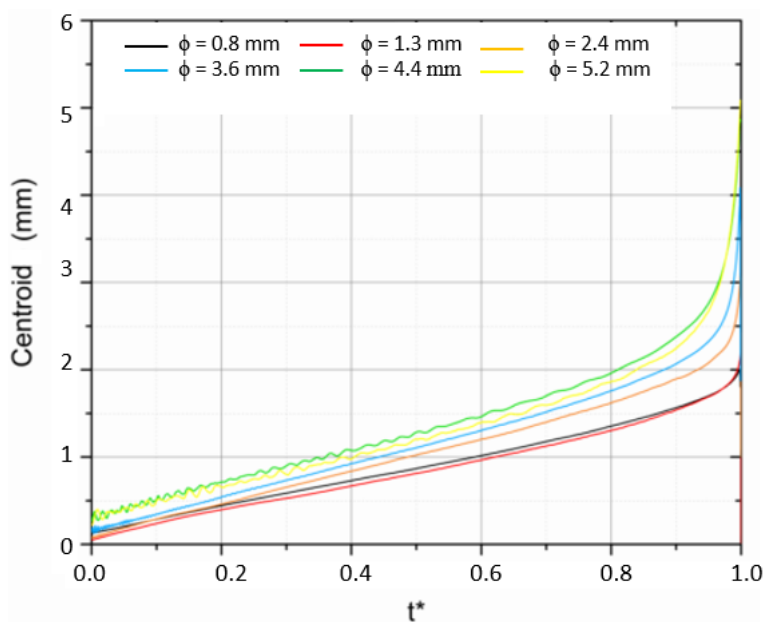


Figure 11. Comparative time evolution of the height of the centroid at departure of the generated bubbles in the superhydrophobic regions with different diameters.

As expected, the values of the height of the centroid of the bubbles at departure were higher for the bubbles nucleated in the larger superhydrophobic spots. However, there were some inconsistent centroid height values during the formation of the bubbles in the different superhydrophobic regions. These discrepancies may have arisen from the developed MATLAB code. The plot in Figure 12 presents the evolution over time of the mean volume of the bubbles.

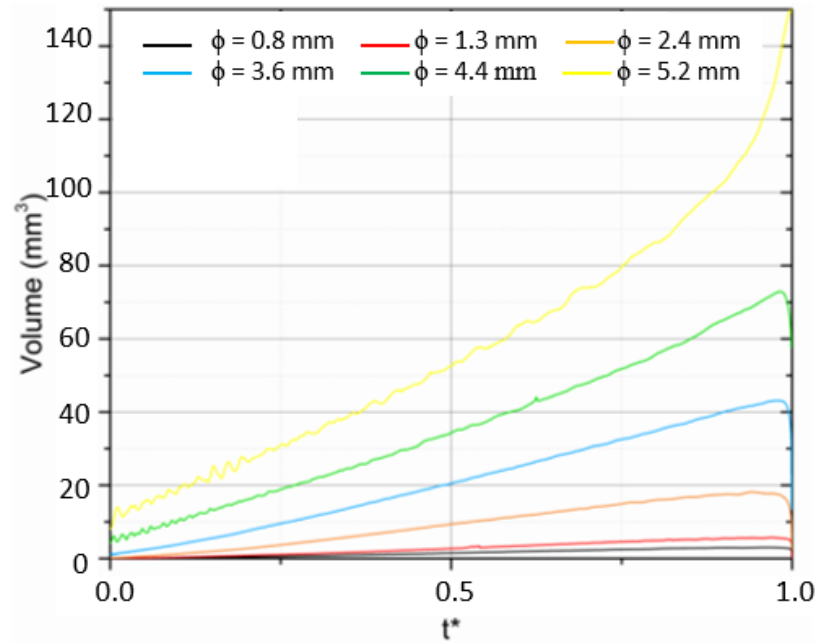


Figure 12. Comparative time evolution of the mean volume at departure of the generated bubbles in the superhydrophobic regions with different diameters.

The plot in Figure 12 clearly shows distinct tendencies in the variation in the mean vapor volume of the bubbles over time, according to the different sizes of the studied superhydrophobic regions. In the larger regions, bigger bubbles with larger base diameters formed, and consequently, they had higher mean volume values in each stage of their generation. It can also be stated that there was a considerable increase in the slope of the curves with the increasing diameter of the superhydrophobic spots. Hence, there was an appreciable difference of around 140 mm^3 between volumes of the bubbles at the departure stage, which were naturally higher for the superhydrophobic spots, with larger diameters and steeper curve slopes. For values of t^* superior to 0.85, we observed a marked instability in the trend lines of the evolution of the volume of the bubbles generated in all the superhydrophobic spots. This instability may be derived from the convective streams inside the boiling chamber, which affected the bubbles with special emphasis at the necking stage when their connection with the surface was more fragile. The necking stage also enhanced the flow effects induced by the convective streams, given that apart from the base necking, the diameter of the bubbles reached its maximum in this final growing stage. Additionally, the next two plots are relative to the comparative evolution of the departure frequency of the bubbles and evaporation mass transfer rate according to the heat flux. The plot in Figure 13 exhibits an increasing mean departure frequency of the bubbles with increasing heat flux. This trend is almost linear for all the evaluated superhydrophobic regions. The smaller superhydrophobic spots naturally promoted the departure of bubbles with smaller diameters, thus enabling higher departure frequencies of the bubbles. In the superhydrophobic region with the smallest diameter, 0.8 mm, the mean departure frequency of the bubbles reached a value superior to 2.5 Hz, whereas the departure frequency in the superhydrophobic region with the largest diameter, 4.4 mm, was of only around 0.25 Hz. In the latter case, we also noticed an increase in the

departure frequency that was higher than that expected. Indeed, for heat fluxes superior to approximately 0.15 W/cm^2 , the mean departure frequency of the bubble generated in the corresponding superhydrophobic spot was higher than the one of the smaller spot with a 3.6 mm diameter. This tendency may be derived from the eventual pressure and temperature fluctuations inside the pool boiling chamber. It should be noted that for a heat flux of 0.03 W/cm^2 , corresponding to an applied electric charge of 3A, it was not possible to observe any bubble nucleation in the largest superhydrophobic region, which indicated that this value of heat flux was still too low to assure a stable bubble nucleation.

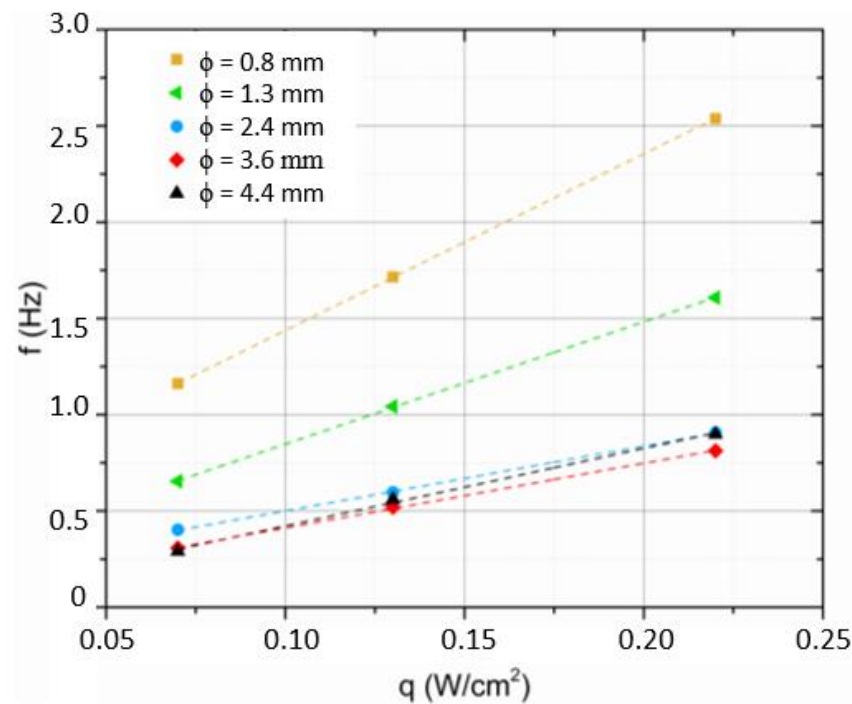


Figure 13. Comparative evolution of the mean departure frequency of the generated bubbles in superhydrophobic regions with different diameters (0.8 mm, 1.3 mm, 2.4 mm, 3.6 mm, and 4.4. mm) according to the imposed heat flux.

It is of relevance to determine the evaporation mass transfer rate of each biphilic surface, given that this parameter is closely linked with the latent heat fraction that can be removed from the heating surface in pool boiling scenarios. In fact, the mechanistic models proposed by Kurul and Podowski [3], for instance, mention that the total heat flux dissipated in pool boiling results from the following fundamental factors: (i) natural convection before the nucleation of the bubbles, (ii) latent heat removed from the surface resulting from the liquid mass evaporation, and (iii) the convection induced by the cooler liquid motion provoked by the displacement of the bubbles during the final stages of development and departure. This last factor can be promoted by the interaction between the bubbles and the nucleation active sites. The evaporation mass transfer rate in each superhydrophobic region can be found using Equation (3):

$$\frac{\dot{m}}{A_{SHF}} = 4 \times \frac{\rho_v \times f \times V_b}{\pi \times \phi^2} \quad (3)$$

where \dot{m} is the evaporation mass per unit of time, A_{SHF} is the area of the superhydrophobic region, ρ_v is the vapor density, f is the departure frequency of the bubbles, V_b is the estimated volume of the bubble, estimated by a spherical approach using the diameter of the bubble at departure, and ϕ is the diameter of the superhydrophobic region. The trend displayed in the plot in Figure 13 is more pronounced in the plot in Figure 14. In the latter, it is possible to observe that the superhydrophobic region with the smallest

diameter, 0.8 mm, presented an evaporation mass transfer rate appreciably higher than the rest of the superhydrophobic regions. Therefore, the superhydrophobic region with smaller dimensions was the one that displayed the best performance and the largest contribution to the latent heat fraction that can be removed from the heating surface.

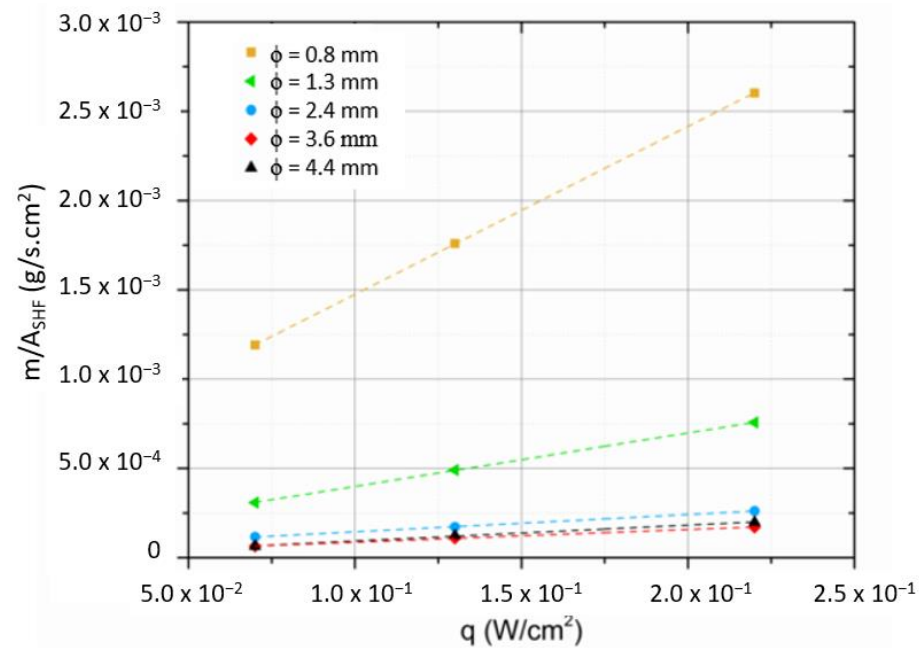


Figure 14. Comparative evolution of the evaporation mass transfer rate per unit of time and area in superhydrophobic regions with different diameters (0.8 mm, 1.3 mm, 2.4 mm, 3.6 mm, and 4.4. mm) according to the imposed heat flux.

Additionally, the linear progress in the plot for each superhydrophobic region confirms the general trend in the evolution of the evaporation mass transfer rate per unit of area according to the heat flux. Hence, the evaporation mass transfer rate decreased with the increasing area of the superhydrophobic regions. For instance, with an imposed heat flux of 0.22 W/cm², the superhydrophobic region with a 0.8 mm diameter presented an evaporation mass transfer rate of around 2.6×10 g/s.cm², which was ten-fold superior to that of the superhydrophobic region with a 2.4 mm diameter. Therefore, in this case, a nine-fold decrease in the superhydrophobic region represented a ten-fold increase in the evaporation mass transfer rate. It can be concluded that the superhydrophobic region with the smallest diameter, 0.8 mm, had the most effective heat transfer area, given that it optimized the evaporation mass transfer rate per unit of area, producing proportionally more vapor than the larger superhydrophobic regions. Although the respective plot is not included in the current work, we also performed a surface temperature evolution over the superhydrophobic regions in the function of the nondimensional position x^* in the central axis of the base of the bubble. The plot was obtained at a t^* of 0.5 and a current intensity of 9A. An analysis of the plot representing the surface temperature evolution showed a decrease in the surface superheating and in the integral temperature oscillations with the decreasing diameter of the superhydrophobic region. This fact reflects the improved uniformization of the temperature of the surface, along with an enhanced stabilization of the nucleate pool boiling in the smaller superhydrophobic regions. In essence, in accord with the results reported by Pontes et al. [14] and in view of the obtained results, it can be concluded that the bubble dynamics are directly influenced by the dimensions of the superhydrophobic spots, mainly because of the effect of the surface tension forces at the boundaries between the hydrophilic base region and the superhydrophobic spots. Moreover, the temperature differences were also found to be greater at the interfacial boundaries between the hydrophilic and superhydrophobic regions and, hence, the smaller superhy-

drophobic regions promoted increased evaporated mass fluxes, increasing the heat fluxes closely linked with the latent heat of evaporation. Considering these facts, the ideal biphilic surface arrangement should exhibit extremely small, millimetric or even micrometric, superhydrophobic spots, which have been demonstrated to achieve higher mass evaporation values in comparison with larger superhydrophobic regions. Additionally, concerning the distance between the superhydrophobic spots, it is recommended to conduct further in-depth experimental works involving influencing factors such as the above-mentioned temperature gradients and the bubble departure dynamics, which promote the flow of the cold liquid in the spaces between the superhydrophobic regions. Nonetheless, the superhydrophobic spots should exhibit enough interspacing to avert the coalescence of the bubbles. If the superhydrophobic spots are not separated by a distance greater than the diameter of the bubbles, as reported by Pontes et al. [32], the bubbles interact and coalesce, forming a bridge between the vapor layers, and, hence, insulating the heat transfer surface between the spots and provoking the deterioration of the pool boiling heat transfer performance.

4. Conclusions

In view of the obtained results, the conclusions of this work can be summarized as follows:

- The results and plots revealed well-defined trends in the bubble dynamics parameters, including the contact angle, base diameter of the bubble, maximum diameter of the bubble, height of the centroid, and volume of the bubble.
- The plots relative to the departure frequency of the bubbles and the evaporation mass transfer rate per unit of area have reinforced the notion that improved heat transfer can be achieved using smaller superhydrophobic regions in the biphilic boiling surface.
- The benefits of using a smaller superhydrophobic spot derive from the existence of a very a small superheat on the spot, and even a smaller superheat in the hydrophilic region, which is the region where the heat dissipates the most. High superheats should be avoided in cooling applications, given that they induce high overall operating temperatures and may cause the overheating of the system. It can be concluded that it is advantageous to use a smaller superhydrophobic spot within reasonable dimensions. There is no need to use a tiny spot, given that there can be assured all the same very small superheats in the hydrophilic region.
- At imposed heat fluxes superior to 1300 w/m^2 , we verified an increased superheat of 11 K in the superhydrophobic region, which is associated with the continuous vapor formation covering the superhydrophobic region, confirming a continuous activation of the superhydrophobic region as a nucleation site. This contrasts with the low superheat which is kept in the hydrophilic region. Playing with this effect one can assure the increase in the heat transfer at an overall low superheat of the biphilic surface, which is the main purpose of its usage in cooling applications.
- We found an exponential evolution of the ratio between the maximum diameter at departure of a bubble and its base diameter in the various superhydrophobic regions.
- The technical capacity limitation of the present study was reached with the superhydrophobic region with a 0.8 mm diameter.
- Another mentionable limitation was the unsuccessful attempt to fabricate biphilic surfaces with multiple superhydrophobic regions with diameters lower than 1 mm. Thus, any thermographic imaging observation and analysis of a biphilic surface with multiple superhydrophobic regions were excluded from this study.
- Further complementary studies involving multiple microscale spots and those smaller than the ones used in this experimental work are expected to be of particular importance.
- We suggest conducting further studies with multiple superhydrophobic spot arrangements to achieve a better understanding of the bubble coalescence effects in the pool boiling heat transfer capability.

- Working fluids other than distilled water should be tested, such as metallic [39], metallic oxide, and graphene oxide [40] nanofluids to evaluate the heat transfer enhancement of the system using the same geometrical configuration.
- Further studies on the durability and performance over time of biphilic surfaces are highly recommended.

Author Contributions: Conceptualization, J.P. and R.C.; methodology, J.P. and A.M. (Ana Moita); software, A.M. (Ana Moita); validation, A.M. (Ana Moita) and A.M. (António Moreira); formal analysis, A.M. (Ana Moita); investigation, J.P.; resources, A.M. (António Moreira); data curation, J.P. and R.C.; writing—original draft preparation, J.P. and R.C.; writing—review and editing, J.P.; supervision, A.M. (Ana Moita) and A.M. (António Moreira); project administration, A.M. (António Moreira); funding acquisition, A.M. (António Moreira). All authors have read and agreed to the published version of the manuscript.

Funding: The authors are grateful to the Fundação para a Ciência e a Tecnologia (FCT), Avenida D. Carlos I, 126, 1249-074 Lisboa, Portugal, for partially financing the Project “Estratégias interfaciais de arrefecimento para tecnologias de conversão com elevadas potências de dissipação”, Ref. PTDC/EMETED/7801/2020, António Luís Nobre Moreira, Associação do Instituto Superior Técnico para a Investigação e o Desenvolvimento (IST-ID). The author José Pereira also acknowledges FCT for his Ph.D. Fellowship Ref. 2021.05830.BD.

Institutional Review Board Statement: Not applicable.

Informed Consent Statement: Not applicable.

Data Availability Statement: Data sharing not applicable.

Conflicts of Interest: The authors declare no conflict of interest.

References

1. Chen, G.; Jia, M.; Zhang, S.; Tang, Y.; Wan, Z. Pool boiling enhancement of novel interconnected microchannels with reentrant cavities for high-power electronics cooling. *Int. J. Heat Mass Transf.* **2020**, *156*, 119836. [[CrossRef](#)]
2. Franci, A.; Onate, E.; Carbonell, J.M.; Chiumenti, M. PFEM formulation for thermo-coupled FSI analysis. Application to nuclear core melt accident. *Comput. Methods Appl. Mech. Eng.* **2017**, *325*, 711–732. [[CrossRef](#)]
3. Raghupathi, P.A.; Kandlikar, S.G. Characterization of Pool Boiling of Seawater and Regulation of Crystallization Fouling by Physical Aberration. *Heat Transf. Eng.* **2017**, *38*, 1296–1304. [[CrossRef](#)]
4. Raj, R.; Kim, J.; McQuillen, J. Pool Boiling Heat Transfer on the International Space Station: Experimental Results and Model Verification. *J. Heat Transf.* **2012**, *134*, 101504. [[CrossRef](#)]
5. Liu, Y.; Olewski, T.; Véchet, L.N. Modeling of a cryogenic liquid pool boiling by CFD simulation. *J. Loss Prev. Process Ind.* **2015**, *35*, 125–134. [[CrossRef](#)]
6. Kang, M.-G. Pool boiling heat transfer from an inclined tube bundle. *Int. J. Heat Mass Transf.* **2016**, *101*, 445–451. [[CrossRef](#)]
7. Halon, T.; Zajackowski, B.; Michaeli, S.; Rulliere, R.; Bonjour, J. Enhanced tunneled surfaces for water pool boiling heat transfer under low pressure. *Int. J. Heat Mass Transf.* **2018**, *116*, 93–103. [[CrossRef](#)]
8. Das, A.K.; Das, P.K.; Saha, P. Performance of different structured surfaces in nucleate pool boiling. *Appl. Therm. Eng.* **2009**, *29*, 3643–3653. [[CrossRef](#)]
9. Choon, N.K.; Chakraborty, A.; Aye, S.M.; Xiaolin, W. New pool boiling data for water with copper-foam metal at sub-atmospheric pressures: Experiments and correlation. *Appl. Therm. Eng.* **2006**, *26*, 1286–1290. [[CrossRef](#)]
10. Shi, T.; Liang, J.; Li, X.; Zhang, H. Improving the Corrosion Resistance of Aluminium Alloy by Creating a Superhydrophobic Surface Structure through a Two-Step Process of Etching Followed by Polymer Modification. *Polymers* **2022**, *14*, 4509. [[CrossRef](#)]
11. Malavasi, I.; Teodori, E.; Moita, A.S.; Moreira, A.L.N.; Marengo, M. Wettability effect on pool boiling: A review. In *Encyclopedia of Two-Phase Heat Transfer and Flow III: Macro and Micro Flow Boiling and Numerical Modeling Fundamentals*; World Scientific Publishing Co., Pte Ltd.: Singapore, 2018; Volume 4. [[CrossRef](#)]
12. Allred, T.P.; Weibel, J.A.; Garimella, S.V. The petal effect of parahydrophobic surfaces offers low receding contact angles that promote effective boiling. *Int. J. Heat Mass Transf.* **2019**, *135*, 403–412. [[CrossRef](#)]
13. Hsu, C.C.; Chen, P.H. Surface wettability effects on critical heat flux of boiling heat transfer using nanoparticle coatings. *Int. J. Heat Mass Transf.* **2012**, *55*, 3713–3719. [[CrossRef](#)]
14. Pontes, P.; Cautela, R.; Teodori, E.; Moita, A.S.; Moreira, A.L.N. Experimental description of bubble dynamics and heat transfer processes occurring on the pool boiling of water on biphilic surfaces. *Appl. Therm. Eng.* **2020**, *178*, 115507. [[CrossRef](#)]
15. Sarode, A.; Raj, R.; Bhargava, A. Effect of confinement and heater surface inclination on pool boiling performance of patterned wettability surfaces. *J. Enhanc. Heat Transf.* **2020**, *27*, 711–727. [[CrossRef](#)]

16. Deng, W.; Ahmad, S.; Liu, H.; Chen, J.; Zhao, J. Improving boiling heat transfer with hydrophilic/hydrophobic patterned flat surface: A molecular dynamics study. *Int. J. Heat Mass Transf.* **2022**, *182*, 121974. [[CrossRef](#)]
17. Azarkish, H. Pool boiling enhancement on biphilic micropillar arrays: Control of the thin film evaporation and rewetting film. *Numer. Heat Transf. Part A Appl.* **2020**, *8*, 60–72. [[CrossRef](#)]
18. Shen, B.; Yamada, M.; Hidaka, S.; Liu, J.; Shiomi, J.; Amberg, G.; Do-Qaung, M.; Kohno, M.; Takahashi, K.; Takata, Y. Early Onset of Nucleate Boiling on Gas-covered Biphilic Surfaces. *Sci. Rep.* **2017**, *7*, 2036. [[CrossRef](#)]
19. Lim, D.Y.; Bang, I.C. Controlled bubble departure diameter on biphilic surfaces for enhanced pool boiling heat transfer performance. *Int. J. Heat Mass Transf.* **2020**, *150*, 119360. [[CrossRef](#)]
20. Jo, H.; Park, H.S.; Kim, M.H. Single bubble dynamics on hydrophobic-hydrophilic mixed surfaces. *Int. J. Heat Mass Transf.* **2016**, *93*, 554–565. [[CrossRef](#)]
21. Betz, A.R.; Xu, J.; Qiu, H.; Attinger, D. Do surfaces with mixed hydrophilic and hydrophobic areas enhance pool boiling? *Appl. Phys. Lett.* **2010**, *97*, 141909. [[CrossRef](#)]
22. Motezakker, A.R.; Sadaghiani, A.K.; Çelik, S.; Larsen, T.; Villanueva, L.G.; Kosar, A. Optimum ratio of hydrophobic to hydrophilic areas of biphilic surfaces in thermal fluid systems involving boiling. *Int. J. Heat Mass Transf.* **2019**, *135*, 164–174. [[CrossRef](#)]
23. Sun, Z.; Chen, X.; Qiu, H. Bubble Dynamics and Heat Transfer During Pool Boiling on Wettability Patterned Surfaces. *Heat Transf. Eng.* **2018**, *39*, 663–671. [[CrossRef](#)]
24. Xia, Y.; Gao, X.; Li, R. Influence of Surface Wettability on Bubble Formation and Motion. *Langmuir* **2021**, *37*, 14483–14490. [[CrossRef](#)] [[PubMed](#)]
25. Serdyukov, V.; Patrin, G.; Malakhov, I.; Surtaev, A. biphilic surface to improve and stabilize pool boiling in vacuum. *Appl. Therm. Eng.* **2022**, *209*, 118298. [[CrossRef](#)]
26. Liu, D.; Li, Y.; Hu, A. Visualization of boiling Heat Transfer on Copper Surface with Different Wettability. *J. Therm. Sci.* **2022**, *31*, 1903–1913. [[CrossRef](#)]
27. Moze, M.; Zupancic, M.; Golobic, I. Pattern geometry optimization on superbiphilic aluminum surfaces for enhanced pool boiling heat transfer. *Int. J. Heat Mass Transf.* **2020**, *161*, 120265. [[CrossRef](#)]
28. Cheng, H.-C.; Jiang, Z.-X.; Chang, T.-L.; Chen, P.-H. Effects of difference in wettability level of biphilic patterns on copper tubes in pool boiling heat transfer. *Exp. Therm. Fluid Sci.* **2021**, *120*, 110241. [[CrossRef](#)]
29. Kamatchi, R.; Venkatachalapathy, S. Parametric study of pool boiling heat transfer with nanofluids for the enhancement of critical heat flux: A review. *Int. J. Therm. Sci.* **2015**, *87*, 228–240. [[CrossRef](#)]
30. Kannan, K.G.; Kamatchi, R. Experimental investigation on thermosiphon aid phase change material heat exchanger for electronic cooling applications. *J. Energy Storage* **2021**, *39*, 102649. [[CrossRef](#)]
31. Valente, T. Study of the Effects of Wettability on Pool Boiling Conditions in a Quiescent Medium. Master's Thesis, Instituto Superior Técnico, Universidade de Lisboa, Lisbon, Portugal, 2015.
32. Pontes, P.; Cautela, R.; Teodori, E.; Moita, A.; Liu, Y.; Moreira, A.L.N.; Nikulin, A.; Barrio, E.P. Effect of pattern geometry on bubble dynamics and heat transfer on biphilic surfaces. *Exp. Therm. Fluid Sci.* **2020**, *115*, 110088. [[CrossRef](#)]
33. Teodori, E.; Palma, T.; Valente, T.; Moita, A.S.; Moreira, A.L.N. Bubble dynamics and heat transfer for pool boiling on hydrophilic, superhydrophobic and biphilic surfaces. *J. Phys. Conf. Ser.* **2016**, *745*, 032132. [[CrossRef](#)]
34. Malavasi, I.; Bourdon, B.; Di Marco, P.; Coninck, J.; Marengo, M. Appearance of a low superheat “quasi-Leidenfrost” regime for boiling on superhydrophobic surfaces. *Int. Commun. Heat Mass Transf.* **2015**, *63*, 1–7. [[CrossRef](#)]
35. Teodori, E.; Valente, T.; Malavasi, I.; Moita, A.S.; Marengo, M.; Moreira, A.L.N. Effect of extreme wetting scenarios on pool boiling conditions. *Appl. Therm. Eng.* **2017**, *115*, 1424–1437. [[CrossRef](#)]
36. Zupancic, M.; Steinbucher, M.; Gregorcic, P.; Golobic, I. Enhanced pool boiling heat transfer on laser-made hydrophobic/superhydrophilic polydimethylsiloxane-silica patterned surfaces. *Appl. Therm. Eng.* **2015**, *91*, 288–297. [[CrossRef](#)]
37. Phan, H.T.; Caney, N.; Marty, P.; Colasson, S.; Gavillet, J. A model to predict the effect of contact angle on the bubble departure diameter during heterogeneous boiling. *Int. Commun. Heat Mass Transf.* **2010**, *37*, 964–969. [[CrossRef](#)]
38. Freitas, E.; Pontes, P.; Cautela, R.; Bahadur, V.; Miranda, J.; Ribeiro, A.P.C.; Souza, R.R.; Oliveira, J.D.; Copetti, J.B.; Lima, R.; et al. Pool Boiling of Nanofluids on Biphilic Surfaces: An Experimental and Numerical Study. *Nanomaterials* **2021**, *11*, 125. [[CrossRef](#)]
39. Kurul, N.; Podowski, M.Z. Multidimensional effects in forced convection subcooled boiling. In Proceedings of the International Heat Transfer Conference, Jerusalem, Israel, 19–24 August 1990; pp. 21–26. [[CrossRef](#)]
40. Kamatchi, R. Experimental investigations on nucleate boiling heat transfer of aqua based reduced graphene oxide nanofluids. *Heat Mass Transf.* **2018**, *54*, 437–451. [[CrossRef](#)]

Disclaimer/Publisher's Note: The statements, opinions and data contained in all publications are solely those of the individual author(s) and contributor(s) and not of MDPI and/or the editor(s). MDPI and/or the editor(s) disclaim responsibility for any injury to people or property resulting from any ideas, methods, instructions or products referred to in the content.